The Astrophysical Journal Letters, 930:L5 (9pp), 2022 May 1 https://doi.org/10.3847/2041-8213/ac651e
© 2022. The Author(s). Published by the American Astronomical Society.
OPEN ACCESS

Observations of a Flare-ignited Broad Quasiperiodic Fast-propagating Wave Train

Xinping Zhou[1,2,3], Yuandeng Shen[1,2,3], Ying D. Liu[2,3], Huidong Hu[2], Jiangtao Su[3,4], Zehao Tang[1,3], Chengrui Zhou[1,3], Yadan Duan[1,3], and Song Tan[1,3]
[1] Yunnan Observatories, Chinese Academy of Sciences, Kunming, 650216, People's Republic of China; ydshen@ynao.ac.cn
[2] State Key Laboratory of Space Weather, Chinese Academy of Sciences, Beijing 100190, People's Republic of China
[3] University of Chinese Academy of Sciences, Beijing 100049, People's Republic of China
[4] National Astronomical Observatories, CAS, Beijing 100101, People's Republic of China
Received 2021 October 10; revised 2022 March 26; accepted 2022 March 29; published 2022 April 29

Abstract

Large-scale extreme-ultraviolet (EUV) waves are frequently observed as an accompanying phenomenon of flares and coronal mass ejections (CMEs). Previous studies mainly focused on EUV waves with single wave fronts that are generally thought to be driven by the lateral expansion of CMEs. Using high spatiotemporal resolution multi-angle imaging observations taken by the Solar Dynamics Observatory and the Solar Terrestrial Relations Observatory, we present the observation of a broad quasiperiodic fast-propagating (QFP) wave train composed of multiple wave fronts along the solar surface during the rising phase of a GOES M3.5 flare on 2011 February 24. The wave train transmitted through a lunate coronal hole (CH) with a speed of $\sim 840 \pm 67$ km s^{-1}, and the wave fronts showed an intriguing refraction effect when they passed through the boundaries of the CH. Due to the lunate shape of the CH, the transmitted wave fronts from the north and south arms of the CH started to approach each other and finally collided, leading to a significant intensity enhancement at the collision site. This enhancement might hint at the occurrence of interference between the two transmitted wave trains. The estimated magnetosonic Mach number of the wave train is about 1.13, which indicates that the observed wave train was a weak shock. Period analysis reveals that the period of the wave train was ~90 s, in good agreement with that of the accompanying flare. Based on our analysis results, we conclude that the broad QFP wave train was a large-amplitude fast-mode magnetosonic wave or a weak shock driven by some nonlinear energy release processes in the accompanying flare.

Unified Astronomy Thesaurus concepts: Solar coronal waves (1995); Alfven waves (23); Solar corona (1483)

Supporting material: animations

1. Introduction

Large-scale propagating wavelike disturbances at fast speeds of 200–1500 km s^{-1} in the solar corona (Nitta et al. 2013) were first observed by the Extreme Ultraviolet Imaging Telescope (EIT; Delaboudinière et al. 1995) on board the Solar and Heliospheric Observatory (SOHO; Domingo et al. 1995), and they were dubbed EIT or extreme-ultraviolet (EUV) waves. During the past two decades, a mass of observational and theoretical studies have been performed to study the origin and physical nature of the EUV waves, and these results indicate that EUV waves could be explained as either fast-mode shock/magnetohydrodynamic (MHD) waves or nonwaves caused by the reconfiguration of coronal magnetic fields (e.g., Vršnak & Cliver 2008; Liu & Ofman 2014). However, no single interpretation can satisfy all constraints imposed by the observations (Long et al. 2017). In order to reconcile the observations, Chen et al. (2002) predicted that there are two types of EUV waves in a solar eruption: a preceding fast-mode shock and a slower wavelike density perturbation caused by the stretching of magnetic field lines. So far, this scenario has been confirmed by many observations (e.g., Chen & Wu 2011; Shen & Liu 2012a; Shen et al. 2014).

Generally, flares and coronal mass ejections (CMEs) are spectacular phenomena that can potentially launch large-scale EUV waves. Thus, there are two main views on the generation of EUV waves. Some researchers favor the idea that EUV waves are generated by the lateral expansion of the associated CMEs (e.g., Chen et al. 2002; Patsourakos et al. 2010; Shen & Liu 2012b; Liu et al. 2019; Downs et al. 2021; Hou et al. 2022). In this view, an EUV wave is generated by the combination of a piston shock and a bow shock owing to the expansion of a CME. Others prefer the idea that the excitation of EUV waves is due to the pressure pulses produced by the accompanying flares (e.g., Khan & Aurass 2002; Warmuth et al. 2004; Magdalenić et al. 2008; Cliver 2016; Kumar et al. 2016). In this view, an EUV wave is driven by the flare volume expansion caused by the impulsive energy release in a flare. Despite a mass of observational and numerical studies that have been performed to support the CME-driven scenario, believable evidence for supporting the flare-driven scenario is still scarce (Vršnak & Cliver 2008). It should be pointed out here that some non-CME-association EUV waves are also not driven by flare pulses. For example, they can be driven by the fast expansion of lower coronal loops associated with failed solar eruptions (e.g., Shen et al. 2017; Zheng et al. 2020) or sudden loop expansion caused by remote eruptions (e.g., Shen et al. 2018d) or coronal jets (e.g., Shen et al. 2018a). Therefore, in the case where an EUV wave is not associated with a CME, one cannot conclude that this EUV wave must be driven by a flare pulse, while other physical mechanisms could still be possible. However, one can check the eruption details with high-resolution imaging observations to clarify the truly driven mechanism of the EUV wave.

Believable evidence for EUV waves driven by flare pulses has been observed by the Atmospheric Imaging Assembly (AIA; Lemen et al. 2012) on board the Solar Dynamics

Original content from this work may be used under the terms of the Creative Commons Attribution 4.0 licence. Any further distribution of this work must maintain attribution to the author(s) and the title of the work, journal citation and DOI.

Observatory (SDO; Pesnell et al. 2012), which are seen as relatively small-scale wave trains along coronal loops and have similar periods as their accompanying flares (e.g., Liu et al. 2011; Shen & Liu 2012c; Shen et al. 2013b, 2018b; Miao et al. 2020, 2021; Zhou et al. 2022). Large-scale quasiperiodic EUV wave trains, similar to typical single-pulsed EUV waves, were also observed ahead of the CME bubble (e.g., Liu et al. 2012). However, the excitation mechanism of these EUV wave trains is still unclear. For example, in Liu et al. (2012), the wave trains have a common 2 minute period with the accompanying flare, while in Shen et al. (2019), the period of the wave trains showed a large difference from that of the accompanying flare. In terms of intuition, such large-scale EUV wave trains are composed of multiple concentric wave fronts, and they are unlikely to be driven by the expansion of CME bubbles. Therefore, Liu et al. (2012) proposed that the EUV wave train was possibly driven by the flare pulse, since its period was similar to the flare. In Shen et al. (2019), since the period of the wave train was similar to the unwinding filament threads in the eruption source region, the authors alternatively proposed that the wave train was excited by the sequentially outward expansion of the unwinding filament threads. As for quasiperiodic fast-propagating (QFP) wave trains, Shen et al. (2022) divided them into narrow and broad QFP types based on their different physical properties. The former is characterized as propagating coherent wave fronts along the coronal loops with a relatively narrow angular width and a small intensity amplitude (Liu et al. 2011; Shen & Liu 2012c; Miao et al. 2019; Zhou et al. 2021; Duan et al. 2022), while the latter propagates along the solar surface with a broad angular width and a relatively large intensity amplitude (Shen et al. 2019). In comparison, the physical parameters of broad QFP wave trains are more similar to the typical single-pulsed EUV waves. The generation mechanism of broad QFP waves is still an open question (Shen et al. 2022), although several numerical simulations have been performed (Yang et al. 2015; Takasao & Shibata 2016; Pascoe et al. 2017; Wang et al. 2021a).

In this letter, we present observations of a broad QFP wave train propagating along the solar surface whose period was similar to the accompanying flare's quasiperiodic pulsations (QPPs). The current event might provide a reliable case for supporting the flare-driven mechanism of the EUV waves. In addition, this study also provides the first evidence of the interference effect of EUV waves, suggesting the true wave nature of the observed disturbance.

2. Results

The broad QFP wave train was intimately associated with a partial halo CME and a GOES M3.5 flare. The CME had an average speed of $\sim$1186 km s^{-1},[5] and the flare's start and peak times were at 07:23 UT and 07:35 UT,[6] respectively. Although the wave train can be identified in all EUV channels of AIA, we concentrate principally on the AIA 171, 193, and 211 Å channels to obtain the essential details of the eruption in this study. In addition, the soft and hard X-ray fluxes recorded, respectively, by GOES and RHESSI (Lin et al. 2002) are also used to analyze the periodicity of the flare QPP.

Figure 1 and the associated animation available in the online journal give an overview of the preeruption configuration and the evolutionary process of the wave train. On 2011 February 24, one can see that the eruption source region (NOAA AR 11163) was located respectively close to the disk center and on the eastern limb from the viewpoints of STEREO-B and the SDO (see Figures 1(a) and (b)). The separation angle between the two spacecraft was $\sim$95°. A low-latitude, lunate coronal hole (CH) can be identified to the west of the eruption source region in the STEREO-B 195 Å images, in which the green curve highlights the boundary of the CH at 07:20:30 UT. The boundary of the CH is also outlined in the AIA 193 Å images and the synoptic maps made from STEREO-B 195 Å and AIA 193 Å running-difference images (see Figures 1(c1)–(c3) and Figure 2). In Figure 1(b), we can see an isolated small CH located to the west of the large lunate CH. Here the synoptic maps are obtained by first transforming the full-disk images into Carrington coordinates and then constructing the synoptic maps. Note that the cadence of the STEREO-B 195 Å images on 2011 February 24 was 5 minutes; therefore, the cadence of the sequence of synoptic maps used to make the animation is 5 minutes.

At 07:30:43 UT, the wave front is exhibited as a bright area with an angle extent of $\sim$270° surrounding the flare kernel (see the red curve in Figure 1(c1)). Since the eruption source region was very close to the eastern boundary of the CH, the wave front began to penetrate into the CH right after its formation, and the westward portion disappeared when it propagated within the CH. At about 07:40:43 UT, the wave front reappeared to the west of the CH (indicated with a blue curve in Figure 1(c3)). This process suggests the transmission of the wave train through the CH. The southward portion of the wave front (indicated by the red curve in Figures 1(c2) and (c3)) showed a free propagation process because no pronounced coronal structures exist in that region. This wave–CH interaction is different from previous observations, where the wave front stopped at the CH boundary and remained stationary for tens of minutes to hours (e.g., Delannée 2000). However, it is similar to the transmission of EUV waves across active regions (ARs; Shen et al. 2013a); in the latter case, the wave front also first disappeared inside the ARs but reappeared at the far-side regions outside the ARs. Such a transmission through ARs or CHs manifests the true wave nature of EUV waves.

The high spatiotemporal resolution AIA images showed more details of the wave train than what was observed in the STEREO-B 195 Å images. The detailed evolution and morphological characteristics are mainly displayed using the running-difference images of AIA 193 and 171 Å in Figure 2, since the evolutionary processes are similar to other wavelength bands. The first wave front clearly appeared at $\sim$07:30:00 UT, about 7 minutes after the start of the accompanying flare (07:23 UT). Then, multiple wave fronts sequentially appeared following the first one with a similar shape. In the quiet-Sun region southeast of the CH, the wave train can be clearly identified in the AIA 193 and 171 Å running-difference images (see the red arrows in Figures 2(a) and (e)). The westward-propagating wave fronts can be identified inside the CH but with a small intensity amplitude in the AIA 171 Å running-difference images (see Figures 2(d) and (e)). However, the simultaneous AIA 193 Å running-difference images did not capture it. This phenomenon might be caused by the lower temperature of the CH that cannot lead

[5] https://cdaw.gsfc.nasa.gov/CME_list/
[6] https://hesperia.gsfc.nasa.gov/goes/goes_event_listings/

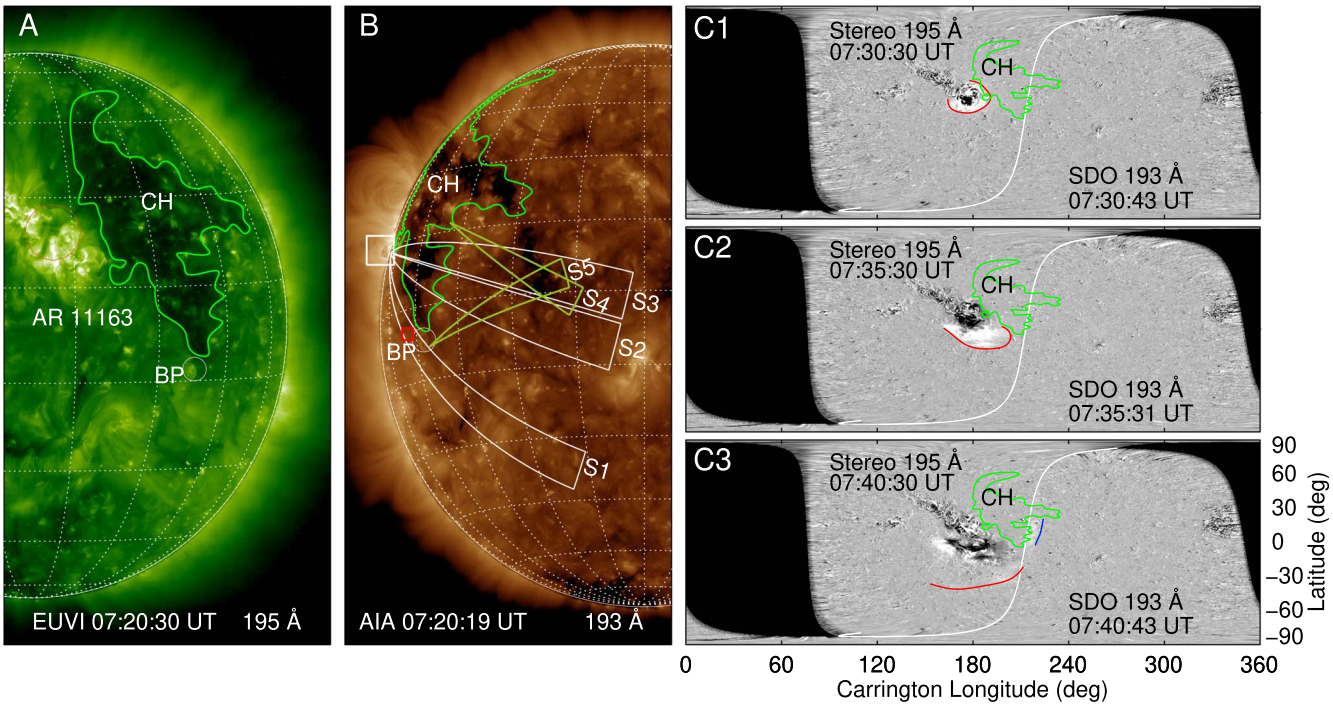

Figure 1. STEREO-B/EUVI 195 Å (a) and SDO/AIA 193 Å (b) direct images showing the flare and initial coronal condition of the eruption source region. The closed region in panel (a) denoted by "CH" represents the coronal hole to the west of the AR in the view of STEREO-B, whose boundary is also projected onto panels (b) and (c1)–(c3) and Figure 2. The spherical sectors S1–S5 in panel (b) are used to obtain time–distance stack plots. The circle denoted by "BP" marks the bright point. The white box in panel (b) is used to collect the AIA light curves shown in Figure 5, while the red box shows the region used to estimate the variation in density and temperature using DEMs in Section 3. The right column shows synoptic maps constructed from running-difference images of EUVI 195 Å and AIA 193 Å. The red and blue lines represent the wave fronts propagated in the quiet Sun and transmitted out of the CH, respectively. The white curves indicate the image boundary observed from the two spacecraft, while the black region is unobserved from the two spacecraft. An animation of panels (c1)–(c3) is available. The animation covers 07:01:55 UT–08:00:19 UT with a 5 minute cadence. In the animation, this sequence appears at the bottom, while the AIA 193 and 171 Å sequence from Figure 2 is shown at the top. The animation duration is 6 s.

(An animation of this figure is available.)

to a significant response in high-temperature 193 Å images (Saqri et al. 2020).

Right after the wave train transmitted through the CH, the wave front reappeared to the west of the CH. At around 07:40:43 UT, one can observe at least two and three wave fronts close to the south and north arms of the CH's western boundary (see the blue arrows in Figure 2(b)). After the transmission, the propagation direction of the transmitted wave fronts showed a significant change; the initial semicircle shape changed to a C-shaped enhanced feature resembling the shape of the western boundary of the CH. The successive refraction should cause a significant change of the propagation direction at the two boundaries of the CH, which acts as a concave lens. Finally, the northern and southern parts of the transmitted wave train propagated toward and interacted with each other in opposite directions (see Figure 2(c)). Interestingly, the interaction of the two transmitted wave trains caused a noticeable intensity enhancement at the collision position. This enhancement could be interpreted as the interference effect between the two wave trains because they originate from the same primary wave train; therefore, they should have the same frequency for satisfying the condition of the occurrence of the interference effect. The interference effect will be discussed in detail in another paper.

To analyze the kinematics of the wave train, we made the time–distance stack plots using the AIA images along five paths as shown in Figure 1(b), in which sectors S1–S3 originate from the flare kernel, while sectors S4 and S5 are along the propagation directions of the south and north transmitted wave trains, respectively. The time–distance stack plots made from AIA 211, 193, and 171 Å running-difference images along S1 are plotted in Figures 3(a)–(c). Since S1 is located in the quiet-Sun region, the wave train initially propagated freely at an average speed of $\sim 668 \pm 24$ km s^{-1}; after the wave train passed through a small bright point (BP) on the path, its speed rapidly increased to more than 845 ± 54 km s^{-1} (see Figures 3(a)–(c)). The time–distance stack plots along sectors S2 and S3 are plotted, respectively, in Figures 3(e)–(g), in which the black dashed line in each panel indicates the western boundary of the CH. In these time–distance stack plots, one can see the significant change of the propagation speed of the wave train at the western boundary of the CH. The speed during the transmission was $\sim 840 \pm 67$ km s^{-1} (see Figure 3(e) and the inset), and it decreased to $\sim 403 \pm 12$ km s^{-1} after the transmission (see Figures 3(e)–(g)).

To study the kinematics of the two transmitted wave trains, we selected two sectors, S4 and S5, along the propagation directions of the wave trains to obtain the time–distance stack plots. The northward- and southward-transmitted wave trains propagated with a similar speed of ~ 400 km s^{-1}, as shown in Figures 3(d) and (h). This value is consistent with the speed of the southern portion of the primary wave train propagated in the quiet-Sun region (along sector S3). After the interference of the two transmitted wave trains, they exhibited as a single observable wave front with a speed of $\sim 485 \pm 25$ km s^{-1} (see Figure 3(f)), slightly higher than those of the transmitted wave

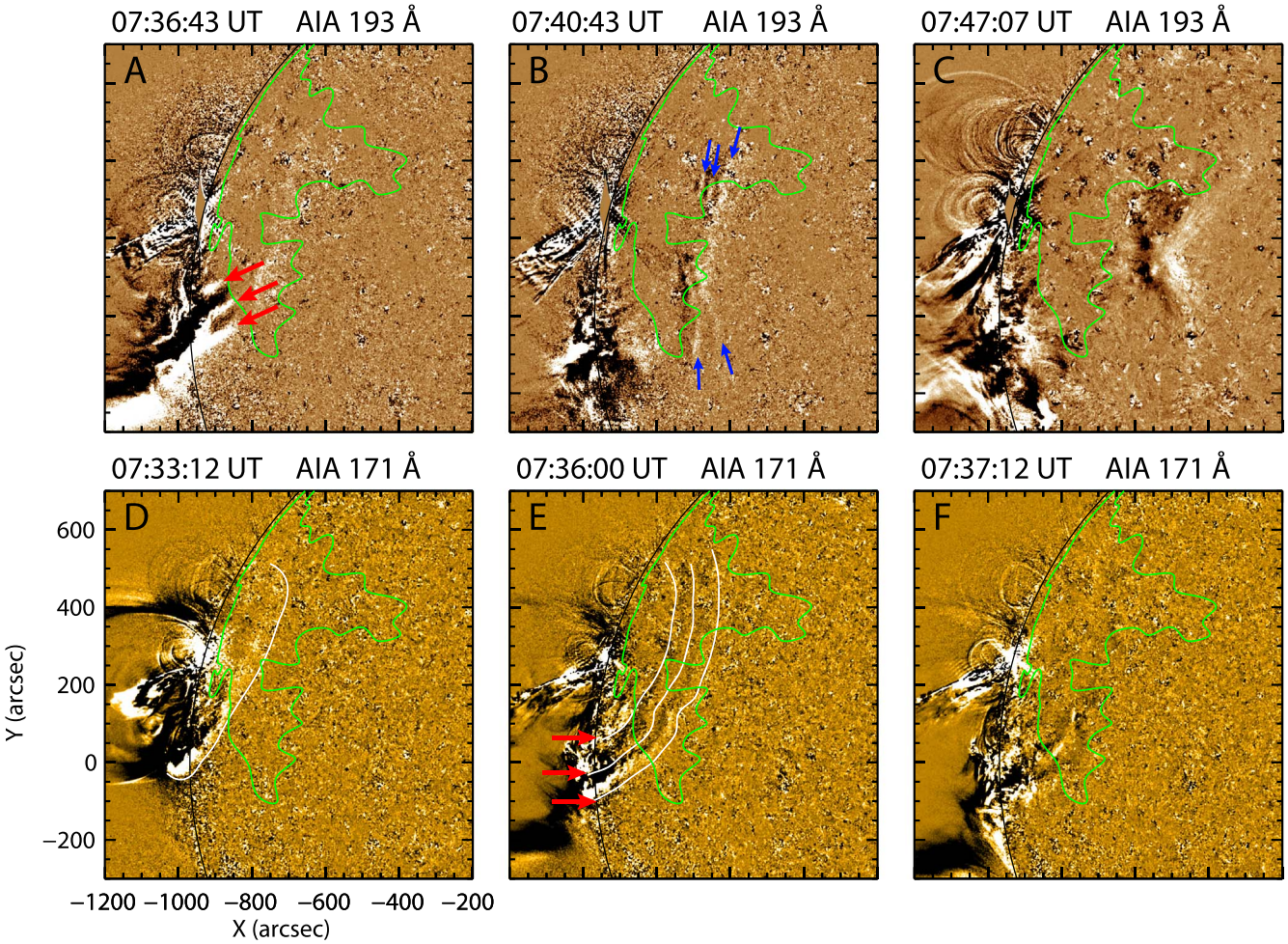

Figure 2. The AIA 193 Å (a)–(c) and 171 Å (d)–(f) running-difference images show the evolution of the wave train. The white curves in panels (d) and (e) tracing the wave front are added to visualize the wave evolution, which is drawn by connecting a sequence of measurement points. The red and blue arrows point to the wave fronts at the different evolutionary stages. The closed region marks the lunate CH boundary. An animation of the evolution of the wave train in 171, 193, and 211 Å (not shown in the figure) is available. This sequence is shown at the top of the animation, while the bottom shows the synoptic maps of Figure 1. The animation covers 07:01:55 UT–08:00:19 UT with a 24 s cadence. The animation duration is 6 s.

(An animation of this figure is available.)

trains. At the same time, a reflected wave was observed between ∼07:46 UT and 08:00 UT at a speed of about 265 ± 24 km s^{-1} (see Figures 3(f) and (g)). The interaction with the small CH to the west of the main CH may be the origin of this reflected wave.

To avoid the influence of the amplitude by the different widths of S1 at different distances, we selected a rectangular slice along the angular bisector of S1 to make a new time–distance stack plot to measure the amplitude of the primary wave train in the quiet-Sun region, and the results are shown in Figure 4(a). Figure 4(b) shows the evolution pattern of the wave train extracted from the running-difference time–distance stack plot at 07:35 UT, in which the blue curve is the corresponding fitting result with a harmonic function. The result indicates that the wave train's wavelength λ was about 58 Mm. In Figure 4(c), we can identify that the relative amplitude intensity is about 35%. These parameters are in agreement with those of broad QFP wave trains (Shen et al. 2019, 2022) and typical single-pulsed EUV waves (Veronig et al. 2010; Warmuth 2015). However, the intensity amplitude is significantly greater than that of the narrow QFP wave train (Shen et al. 2022).

To analyze the periodicity of the flare pulsation, we studied the accompanying flare by using the hard and soft X-ray fluxes recorded by the RHESSI and GOES satellites and the intensity of the light curves measured from the AIA images around the flaring kernel (see Figures 5(a)–(c)). During the impulsive rising phase of the flare (07:24 UT–07:35 UT), as indicated by the vertical dashed lines in Figure 5(c), there are at least four distinct bumps that can be identified in the AIA 171 and 304 Å light curves in Figure 5(b). In the meantime, similar bumps can also be observed in the derivative curve of the GOES 1–8 Å soft X-ray flux (see Figure 5(c)) and the RHESSI 25–50 and 50–100 keV energy bands (see Figure 5(a)). Generally, the appearance of these bumps may manifest the periodic energy release process in the flare. Detailed estimation suggests that the average period of these bumps was about ∼90 s. We further analyzed the periodicity of the wave train and the accompanying flare using the wavelet technique (Torrence & Compo 1998) that has been widely used to analyze the periodicity of time-dependent one-dimensional data. In our analysis, we choose the Morlet function as the mother function in the wavelet software, and the results are shown in Figures 5(d1)–(e3). To analyze the period of the wave train, we extracted the intensity profile

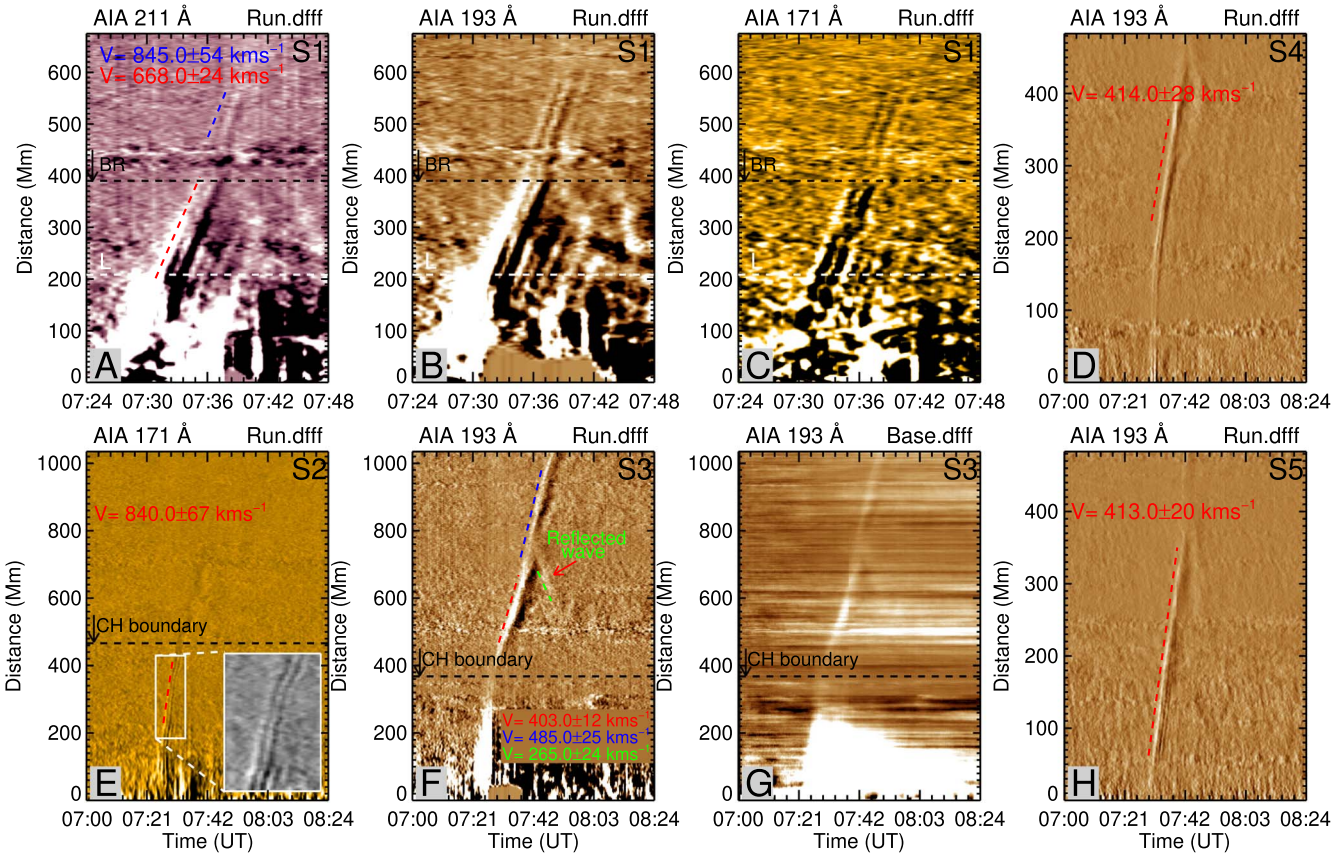

Figure 3. Panels (a)–(c) are time–distance stack plots respectively obtained from AIA 211, 193, and 171 Å running-difference images along sector S1 located in the quiet Sun. The white dashed lines in panels (a)–(c) point to the positions where the intensity profile is used to analyze the periodicities of the wave train, while the black dashed lines indicate the location of the BP. Panels (e)–(g) are running- (panels (e) and (f)) and base-difference (panel (g)) images created along sectors S2 and S3, in which the black dashed lines mark the location of the far-side CH boundary, and the inset in panel (e) is an enlarged view of the wave train inside the CH. Panels (d) and (h) show the evolution of two refracted waves propagated along sectors S4 and S5. The speeds in the different stages are listed in each corresponding panel with different colors.

along the horizontal white dotted lines marked with L from the time–distance stack plots in Figures 3(a)–(c), and the corresponding wavelet power maps are shown in Figures 5(d1)–(d3). Clearly, the main period of the wave train was about ∼90 s. Interestingly, using the relation $v_{\rm ph} = \frac{\lambda}{P}$, we get a phase speed of about 644 km s^{-1}, which is consistent with that obtained from the time–distance stack plots as shown in Figures 3(a)–(c). This result further implies that the observed EUV waves are nondispersive in their formation heights corresponding to the AIA channels, similar to the QFP wave confined in the loop system (Liu et al. 2011). The RHESSI hard X-ray flux curves are used to investigate the period of the flare pulsations, since they represent the nonthermal emissions produced by high-energy particles. Figures 5(e1)–(e3) show the wavelet power maps obtained based on the high-energy bands of RHESSI 12–25, 25–50, and 50–100 keV, respectively. It is clear that the period of the flare pulsations was also ∼90 s, which is in good agreement with that of the observed wave train. It should be pointed out that the main periods (errors) of the wave train and flare were determined by the peak (FWHM) of the corresponding global wavelet power spectra. The common 90 s periodicities of the wave train and the accompanying flare strongly suggest that the two different phenomena should originate from the same physical process, such as the nonlinear magnetic reconnection process in the flare (Shen et al. 2022).

3. Plasma Diagnostics

In this section, we study the variations of the plasma temperature and density during the passage of the wave train. The temperature distribution of the contributing plasma in the line of sight is characterized by the differential emission measure (DEM) for optically thin emission lines from plasma in thermodynamic equilibrium. The DEM is defined as

$$\mathrm{DEM}(T) = n_e^2(T)\frac{dh}{dT}, \quad (1)$$

where n_e is the number density dependent on the temperature T along the line of sight. This method enables a direct estimation of the variations of the coronal density and temperature during the wave's passage. To quantify the variations of temperature and density in the region highlighted with a red box in Figure 1(b), the DEM of the plasma observed by SDO/AIA was estimated using the inversion code developed by Hannah & Kontar (2012). The DEM inversion was done between 07:27 UT and 07:50 UT. Following Cheng et al. (2012) and Vanninathan et al. (2015), the average temperature and density can be defined as

$$\bar{T} = \frac{\int_T \mathrm{DEM}(T)TdT}{\int_T \mathrm{DEM}(T)dT} \quad (2)$$

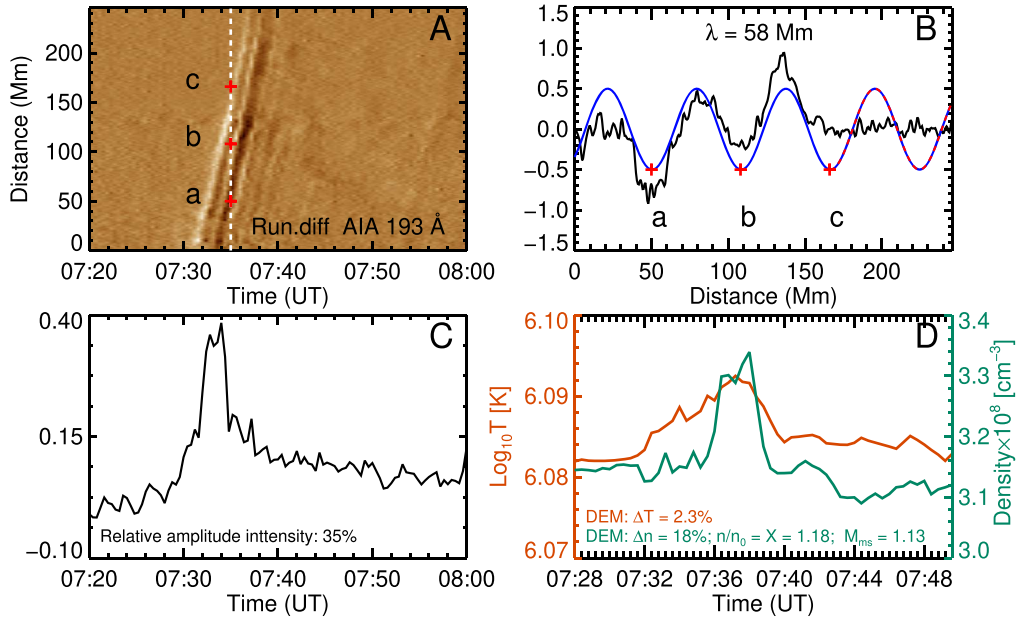

Figure 4. Panel (a) shows the running-difference time–distance stack plot of 193 Å along a rectangular slice (not shown here) that tracked the angular bisector of sector S1. Note that the starting point of the y-axis is not at the flare kernel. Panel (b) shows the profile of the wave front at 07:35 UT, indicated as the vertical white line in panel (a), in which the red plus signs, corresponding the location of the red plus signs in panel (a), mark the positions of the trough at a distance of 50, 108, and 166 Mm, respectively. The blue curve in panel (b) is the result of fitting the wave profile using the harmonic function, which shows the wavelength of 58 Mm. Panel (c) shows the time profile of the relative amplitude extracted from the position 50 Mm in a base-difference stack plot, as shown in panel (a). Panel (d) shows the variation in density (green) and temperature (orange) estimated in the region outlined by the red box in Figure 1(b) using the DEM version developed by Hannah & Kontar (2012). The percentage increase in density and temperature due to the wave's passage and the magnetosonic Mach number estimated using Equation (4) are shown in the figure.

and

$$\bar{n} = \sqrt{\frac{\int_T \mathrm{DEM}(T)\,dT}{h}}, \tag{3}$$

respectively, where h is the column height of the emitting plasma along the line of sight taken as 90 Mm (see Patsourakos & Vourlidas 2009; Long et al. 2021). As shown in Figure 4(d), both the temperature (orange) and the density (green) exhibit an increase as a result of the wave's passage, with gains of 2.3% and 18%. These variations in temperature and density are consistent with the report of Vanninathan et al. (2015) and Long et al. (2021). Since the measured intensity of the EUV images is a function of both the temperature and the density, the small percentage increase in temperature indicates that the measured EUV intensity variation is mainly due to the change of the plasma density rather than the temperature.

Assume that the observed wave train propagated perpendicular to the direction of the magnetic field (see Vršnak et al. 2002; Long et al. 2021); this is reasonable, since the magnetic field in the quiet-Sun corona has a strong vertical component. The magnetosonic Mach number M_{ms} can be calculated using

$$M_{\mathrm{ms}} = \sqrt{\frac{X(X+5+5\beta)}{(4-X)(2+5\beta/3)}}, \tag{4}$$

where X is the density compression ratio, defined as $X = n/n_0$, and β is the plasma-β (here taken as 0.1 following Muhr et al. 2011). The M_{ms} is 1.13 when taking the density compression ratio of 1.18 estimated by the DEM, suggesting that the observed wave train was weakly shocked.

4. Discussions and Conclusions

By combining the high spatiotemporal resolution and multiple-angle observations taken by SDO and STEREO-B, we studied the generation mechanism and propagation behaviors of a broad QFP wave train in association with a GOES M3.5 flare and a partial halo CME on 2011 February 24. Based on our analysis results, we propose that the observed QFP wave train was probably driven by the pressure pulses caused by the intermittent energy release in the accompanying flare. In addition, for the first time, we reported the transmission of the wave train through a low-latitude CH and the interference effect between the transmitted wave trains. The high projection speed (668 ± 24 km s^{-1}), Mach number (1.13), transmission phenomenon, and interference effect of the wave train together suggest that the observed wave train should be a fast-mode magnetosonic wave or a weak shock. In addition, based on the DEM estimation, we find that both the corona's density and the temperature increased after the passage of the wave train, which might indicate the heating of coronal plasma by the wave.

We studied the complete transmission process of the QFP wave train through the CH, although the wave signal was very weak with respect to that in the quiet Sun. The speed of the wave train during the transmission was $\sim 840 \pm 67$ km s^{-1}, which is $\sim$20% faster than that in the quiet-Sun region. This result is consistent with previous observations and simulations; i.e., the velocity of fast-mode magnetosonic waves propagating inside strong magnetic field strength regions such as CHs and ARs is faster than that in the quiet-Sun region (Gopalswamy et al. 2009; Schmidt & Ofman 2010; Olmedo et al. 2012; Hu et al. 2019). The faster magnetosonic wave speeds inside CHs are due to the higher magnetic field strength and lower plasma density inside CHs; such characteristics of CHs can lead to a

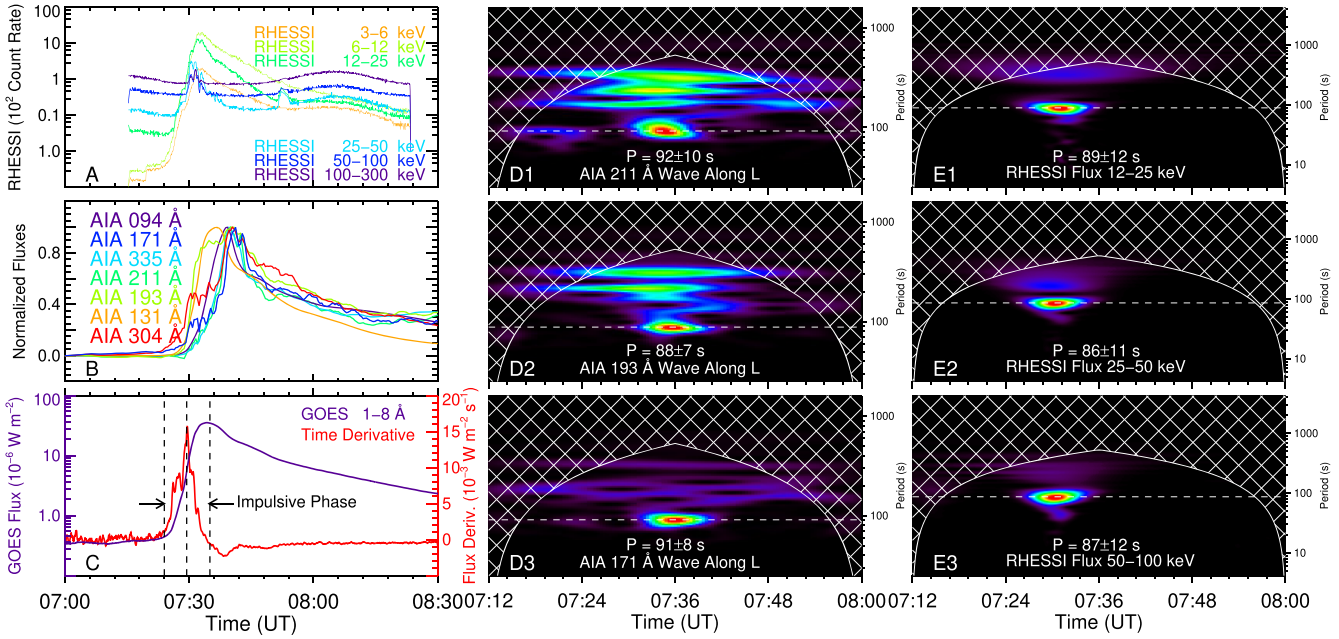

Figure 5. Panels (a) and (b) are the RHESSI hard X-ray fluxes and normalized light curves within the eruption source region as outlined by the white box in Figure 1(b) measured from different AIA channels, respectively. Panel (c) shows the GOES 1–8 Å flux (purple) and its derivative curve (red). The middle column (panels (d1)–(d3)) shows the power maps of detrended intensity profiles along the horizontal white dashed lines as shown in Figures 3(a)–(c), while the right column (panels (e1)–(e3)) shows the wavelet power maps of RHESSI hard X-ray fluxes in the energy band of 12–100 keV. In each wavelet power map, the period is highlighted by a white horizontal dashed line, and the corresponding period P is also listed in the figure.

higher Alfvén speed inside CHs than in the quiet-Sun region. The intensity amplitude of the wave train was reduced significantly inside the CH compared to that in the quiet-Sun region. This result can be interpreted as the result of the conservation of energy (Downs et al. 2021); i.e., as an EUV wave enters a strong magnetic field region (such as a CH) from a weak magnetic field region (such as the quiet-Sun region), the leading part of the wave front speeds up, but the trailing part does not, which naturally results in the widening of the perturbation profile and therefore the decrease of the intensity amplitude. In general, the kinetic energy of a wave is directly proportional to the integral of the mass density and the square of the wave amplitude over the whole wave packet. In addition, we find that the wave train had an elevated speed of 845 km s^{-1} after its passage through the small BP, as in the results reported in Shen & Liu (2012b) and Hu et al. (2019). This may be due to the refraction of the wave after passing through the BP, resulting in an increase in its projection velocity. After leaving the western boundary of the CH, the intensity of the wave front was significantly enhanced at the location where the south-westward- and northeastward-propagating transmitted wave fronts collided head-on. We propose that the amplitude enhancement was caused by the interference between the two transmitted wave trains. This explanation is reasonable because the two transmitted wave trains were separated from the same wave train; therefore, they had the same frequency as the primary wave train. These conditions provide the necessary physical premise for the occurrence of the interference effect. We believe the enhancement results from the interference effect. The ideal situation is that the southern wave train propagates toward the north, while the northern wave train propagates toward the south, after the interference effect. However, the actual problem is that the waves themselves have become very weak after propagating a long distance, which leads to the observed wave looking like a single wave front after the collision. In this event, the wave train propagated at a fast magnetosonic wave speed, exhibiting refraction, reflection, transmission, and interference effects. These characteristics strongly suggest that the observed wave train should be a fast-mode MHD wave in nature. The wave train propagated along the solar surface with an angular extent of about 270° and a relative maximum intensity amplitude of about 35% relative to the unperturbed background corona. These parameters are significantly larger than the QFP wave trains along open or closed coronal loops (i.e., narrow QFP wave trains), where the angular width and maximum intensity amplitude are in the range of 10°–60° and 1%–5%, respectively (Liu & Ofman 2014; Shen et al. 2022). These differences suggest that the observed wave train belongs to the broad type of QFP wave train, as proposed in Shen et al. (2022), which has a relatively larger intensity amplitude, higher energy flux, and larger angular extent than narrow QFP wave trains along coronal loops. The magnetosonic Mach number M_{ms} of the observed wave train is about 1.13, which suggests that it should be a nonlinear fast-mode magnetosonic wave or a weak shock.

A study of the relationship among flares, CMEs, and waves is essential for diagnosing the generation mechanism of EUV waves. Generally, there are two competing candidate drivers for EUV waves, namely, flares and CMEs. One of the main reasons for the controversy about the origin of coronal waves is the synchronization of the CME acceleration phase and the impulsive phase of the associated flare (Zhang et al. 2004; Liu et al. 2014). Therefore, it is hard to distinguish whether a particular EUV wave is driven by a CME or ignited by a flare. Considering 100 Mm was confirmed as a typical distance (i.e., the distance of the earliest observed wave front from the extrapolated radiant point) for the appearance of a coronal wave (Veronig et al. 2008; Warmuth & Mann 2011; Shen & Liu 2012a), we estimated that the start time of the first wave front was about 07:28 UT, which was derived from extending

the red line in Figure 3(a) down to a distance of 100 Mm. Actually, the start time of the first wave should be slightly earlier than 07:28 UT because the eruption source was slightly behind the solar disk from the perspective of the SDO. We selected an azimuthal path above the limb to get the information on the CME acceleration phase using the SDO/AIA data. The result indicates that the start time of the CME's acceleration phase was ~07:30 UT, which was behind the start time of 07:28 UT of the first wave. In contrast, the start time of the wave train was ~2 minutes behind the onset of the flare QPPs (07:26 UT; see Figures 5(e1)–(e3)). This time delay is reasonable for a wave train generated by flare QPPs because the first wave was detected at a region far away from the flare source. Although these estimated times have large errors, they can still roughly reflect the relationship between the CME, flare, and wave in time. Therefore, we believe the wave train should be triggered by the accompanying flare, rather than the CME. Recent studies have also found that coronal jets can also launch large-scale EUV waves directly ahead of the jet top (Shen et al. 2018a) and indirectly caused by a sudden expansion of nearby coronal loops through jet–loop interaction (Shen et al. 2018c, 2018d). In the scenario of piston-driven shocks, the piston (CME) can generate a shock wave ahead of the driver, and the wave will freely propagate once it decouples from the CME. However, such EUV waves often show only one wave front in many observations. Therefore, it is hard to understand how a single CME can produce a wave train with multiple coherent wave fronts. In this line of thought, we prefer to propose that the present wave train did not drive by the associated CME. On the other hand, the light curves based on the EUV observations of AIA and hard X-ray fluxes in high-energy bands (12–100 keV) based on the RHESSI observations indicate that the period of the wave trains was consistent with that of the flare QPP. This result strongly suggests that the generation of the wave train was probably caused by the intermittent energy release process in the flare.

Flare QPPs are defined as periodic intensity variations of flare light curves with characteristic periods ranging from a fraction of a second to several tens of minutes (Li et al. 2020a, 2020b, 2021) and have two possible mechanisms: the intermittent energy release/reconnection and MHD oscillations (Nakariakov et al. 2019; Wang et al. 2021b). Observationally, some periods of QFP wave trains are found to be consistent with QPPs, suggesting their common origins. Many numerical simulations based on magnetic reconnection successfully reproduce the broad QFP wave trains with physical parameters consistent with observations, such as morphology, intensity amplitude, period, and speed. In the simulation of Yang et al. (2015) based on the interchange reconnection, multiple wave trains were consecutively launched from the outflow region due to the collision between the plasmoids and the field in the outflow region. As the authors mentioned, the simulated wave train propagates isotropically from the source with a speed of 1000 km s^{-1}, rather than being constrained in funnels with narrow angular extents. Using two-dimensional MHD simulation, Takasao & Shibata (2016) revealed that the waves could be spontaneously generated by the oscillations of the strong magnetic field due to quasi-steady impingement of the reconnection outflow. The exciting process is similar to the sound generated by an externally driven tuning fork. Wang et al. (2021a) reproduced the broad QFP wave train through a three-dimensional radiative MHD simulation. In that simulation, the wave train with a dome shape propagated perpendicular to the magnetic field lines with a speed of ~550–700 km s^{-1}, similar to that of the wave train reported here. The authors proposed that the QFP wave train was possibly driven by the QPP energy release in the accompanying flare. These simulations provided additional evidence that intermittent energy release mechanisms do excite broad QFP wave trains. However, it is necessary to appreciate that the igniting mechanism of the broad QFP wave trains may be diverse and intricate, for example, in the case reported by Shen et al. (2019), the periods of the wave train are completely unassociated with the accompanying flares and are instead consistent with the unwinding of helical structures of filament indicating that the unwinding of filament could drive the wave trains. Pascoe et al. (2017) proposed that the broad QFP wave trains are possibly generated by the leaky components of the impulsively generated wave trains.

We would like to thank the anonymous referee for the many valuable suggestions and comments for improving the quality of this paper, and we are thankful for the data support from the SDO, GOES, and SOHO science teams. This work is supported by the Natural Science Foundation of China (11922307, 12173083, 11773068, 41774179, 11633008, 42004145), the Yunnan Science Foundation for Distinguished Young Scholars (202101AV070004), the National Key R&D Program of China (2019YFA0405000), the Specialized Research Fund for State Key Laboratories, and the West Light Foundation of the Chinese Academy of Sciences.

ORCID iDs

Xinping Zhou https://orcid.org/0000-0001-9374-4380
Yuandeng Shen https://orcid.org/0000-0001-9493-4418
Ying D. Liu https://orcid.org/0000-0002-3483-5909
Huidong Hu https://orcid.org/0000-0001-8188-9013
Jiangtao Su https://orcid.org/0000-0002-5152-7318
Zehao Tang https://orcid.org/0000-0003-0880-9616
Yadan Duan https://orcid.org/0000-0001-9491-699X

References

Chen, P. F., Wu, S. T., Shibata, K., & Fang, C. 2002, ApJL, 572, L99
Chen, P. F., & Wu, Y. 2011, ApJL, 732, L20
Cheng, X., Zhang, J., Saar, S. H., & Ding, M. D. 2012, ApJ, 761, 62
Cliver, E. W. 2016, ApJ, 832, 128
Delaboudinière, J. P., Artzner, G. E., Brunaud, J., et al. 1995, SoPh, 162, 291
Delannée, C. 2000, ApJ, 545, 512
Domingo, V., Fleck, B., & Poland, A. I. 1995, SoPh, 162, 1
Downs, C., Warmuth, A., Long, D. M., et al. 2021, ApJ, 911, 118
Duan, Y., Shen, Y., Zhou, X., et al. 2022, ApJL, 926, L39
Gopalswamy, N., Yashiro, S., Temmer, M., et al. 2009, ApJL, 691, L123
Hannah, I. G., & Kontar, E. P. 2012, A&A, 539, A146
Hou, Z., Tian, H., Wang, J.-S., et al. 2022, ApJ, 928, 98
Hu, H., Liu, Y. D., Zhu, B., et al. 2019, ApJ, 878, 106
Khan, J. I., & Aurass, H. 2002, A&A, 383, 1018
Kumar, P., Innes, D. E., & Cho, K.-S. 2016, ApJ, 828, 28
Lemen, J. R., Title, A. M., Akin, D. J., et al. 2012, SoPh, 275, 17
Li, D., Ge, M., Dominique, M., et al. 2021, ApJ, 921, 179
Li, D., Li, Y., Lu, L., et al. 2020a, ApJL, 893, L17
Li, D., Lu, L., Ning, Z., et al. 2020b, ApJ, 893, 7
Lin, R. P., Dennis, B. R., Hurford, G. J., et al. 2002, SoPh, 210, 3
Liu, R., Wang, Y., & Shen, C. 2014, ApJ, 797, 37
Liu, W., & Ofman, L. 2014, SoPh, 289, 3233
Liu, W., Ofman, L., Nitta, N. V., et al. 2012, ApJ, 753, 52
Liu, W., Title, A. M., Zhao, J., et al. 2011, ApJL, 736, L13
Liu, Y. D., Zhu, B., & Zhao, X. 2019, ApJ, 871, 8
Long, D. M., Bloomfield, D. S., Chen, P. F., et al. 2017, SoPh, 292, 7

Long, D. M., Reid, H. A. S., Valori, G., & O'Kane, J. 2021, ApJ, 921, 61
Magdalenić, J., Vršnak, B., Pohjolainen, S., et al. 2008, SoPh, 253, 305
Miao, Y., Liu, Y., Elmhamdi, A., et al. 2020, ApJ, 889, 139
Miao, Y. H., Liu, Y., Shen, Y. D., et al. 2019, ApJL, 871, L2
Miao, Y., Li, D., Yuan, D., et al. 2021, ApJL, 908, L37
Muhr, N., Veronig, A. M., Kienreich, I. W., Temmer, M., & Vršnak, B. 2011, ApJ, 739, 89
Nakariakov, V. M., Kolotkov, D. Y., Kupriyanova, E. G., et al. 2019, PPCF, 61, 014024
Nitta, N. V., Schrijver, C. J., Title, A. M., & Liu, W. 2013, ApJ, 776, 58
Olmedo, O., Vourlidas, A., Zhang, J., & Cheng, X. 2012, ApJ, 756, 143
Pascoe, D. J., Goddard, C. R., & Nakariakov, V. M. 2017, ApJL, 847, L21
Patsourakos, S., & Vourlidas, A. 2009, ApJL, 700, L182
Patsourakos, S., Vourlidas, A., & Stenborg, G. 2010, ApJL, 724, L188
Pesnell, W. D., Thompson, B. J., & Chamberlin, P. C. 2012, SoPh, 275, 3
Saqri, J., Veronig, A. M., Heinemann, S. G., et al. 2020, SoPh, 295, 6
Schmidt, J. M., & Ofman, L. 2010, ApJ, 713, 1008
Shen, Y., Chen, P. F., Liu, Y. D., et al. 2019, ApJ, 873, 22
Shen, Y., & Liu, Y. 2012a, ApJL, 752, L23
Shen, Y., & Liu, Y. 2012b, ApJ, 754, 7
Shen, Y., & Liu, Y. 2012c, ApJ, 753, 53
Shen, Y., Liu, Y., Liu, Y. D., et al. 2018a, ApJ, 861, 105
Shen, Y., Liu, Y., Song, T., & Tian, Z. 2018b, ApJ, 853, 1
Shen, Y., Liu, Y., Su, J., et al. 2013a, ApJL, 773, L33
Shen, Y., Liu, Y., Tian, Z., & Qu, Z. 2017, ApJ, 851, 101
Shen, Y., Liu, Y. D., Chen, P. F., & Ichimoto, K. 2014, ApJ, 795, 130
Shen, Y., Tang, Z., Li, H., & Liu, Y. 2018c, MNRAS, 480, L63
Shen, Y., Tang, Z., Miao, Y., Su, J., & Liu, Y. 2018d, ApJL, 860, L8
Shen, Y., Zhou, X., Duan, Y., et al. 2022, SoPh, 297, 20
Shen, Y. D., Liu, Y., Su, J. T., et al. 2013b, SoPh, 288, 585
Takasao, S., & Shibata, K. 2016, ApJ, 823, 150
Torrence, C., & Compo, G. P. 1998, BAMS, 79, 61
Vanninathan, K., Veronig, A. M., Dissauer, K., et al. 2015, ApJ, 812, 173
Veronig, A. M., Muhr, N., Kienreich, I. W., Temmer, M., & Vršnak, B. 2010, ApJL, 716, L57
Veronig, A. M., Temmer, M., & Vršnak, B. 2008, ApJL, 681, L113
Vršnak, B., & Cliver, E. W. 2008, SoPh, 253, 215
Vršnak, B., Warmuth, A., Brajša, R., & Hanslmeier, A. 2002, A&A, 394, 299
Wang, C., Chen, F., & Ding, M. 2021a, ApJL, 911, L8
Wang, T., Ofman, L., Yuan, D., et al. 2021b, SSRv, 217, 34
Warmuth, A. 2015, LRSP, 12, 3
Warmuth, A., & Mann, G. 2011, A&A, 532, A151
Warmuth, A., Vršnak, B., Magdalenić, J., Hanslmeier, A., & Otruba, W. 2004, A&A, 418, 1117
Yang, L., Zhang, L., He, J., et al. 2015, ApJ, 800, 111
Zhang, J., Dere, K. P., Howard, R. A., & Vourlidas, A. 2004, ApJ, 604, 420
Zheng, R., Chen, Y., Wang, B., & Song, H. 2020, ApJ, 894, 139
Zhou, X., Shen, Y., Su, J., et al. 2021, SoPh, 296, 169
Zhou, X., Shen, Y., Tang, Z., et al. 2022, A&A, 659, A164